



OPEN

Observation of resonant exciton and correlated plasmon yielding *correlated* plexciton in amorphous silicon with various hydrogen content

Soni Prayogi^{1,2}, Retno Asih¹, Budhi Priyanto¹, Malik A. Baqiya¹, Muhammad A. Naradipa³, Yoyok Cahyono¹, Darminto¹✉ & Andriwo Rusydi^{3,4}✉

Hydrogenated amorphous silicon (a-Si: H) has received great attention for rich fundamental physics and potentially inexpensive solar cells. Here, we observe new resonant excitons and correlated plasmons tunable via hydrogen content in a-Si: H films on *Indium Tin Oxide* (ITO) substrate. Spectroscopic ellipsometry supported with *High Resolution-Transmission Electron Microscopy* (HR-TEM) is used to probe optical properties and the density of electronic states in the various crystallinity from nano-size crystals to amorphous a-Si: H films. The observed optical and electronic structures are analyzed by the second derivative with analytic critical-point line shapes. The complex dielectric function shows good agreement with microscopic calculations for the energy shift and the broadening inter-band transitions based on the electron–hole interaction. Interestingly, we observe an unusual spectral weight transfer over a broad energy range revealing electronic correlations that cause a drastic change in the charge carrier density and determine the photovoltaic performance. Furthermore, the interplay of resonant excitons and correlated plasmons is discussed in term of a correlated plexciton. Our result shows the important role of hydrogen in determining the coupling of excitons and plasmons in a-Si: H film for photovoltaic devices.

Hydrogenated amorphous silicon (a-Si: H) has recently emerged as a favorite material for making large-area thin film-based optoelectronic devices such as thin film solar cells¹, radiation detectors², image sensors³, thin film transistors⁴, memory devices⁵, and microchannel plates on both rigid⁶ and flexible substrate⁷. Besides being inexpensive, environmentally friendly, and non-toxic, this type of material is important because it can be n-type and p-type doped^{8–10} and the p–i–n homo junction structure has been realized without the band gap discontinuity at the interface^{11–13}. Numerous studies have shown the presence of weak Si–Si bonds, Si–H₂ bonds, and cavities that change a-Si: H optoelectronic properties^{14–17}.

Electron–hole interactions, known as an exciton, play an important role in semiconductor and photovoltaic devices^{18–20}. A dilution of hydrogen from the process gas mixture of silane and hydrogen has been used to improve the stability of a-Si: H materials and devices²¹. Recent results suggest that a significant increase in the stability of a-Si: H cell occurs when the intrinsic layer is created from a gas mixture diluted with hydrogen^{22–24}. While the hydrogen content of this material is similar to alloys made with low hydrogen dilution, the effusion of hydrogen from this film occurs at a much lower temperature^{25,26}. Besides, in the presence of electron excitation or thermal stimulation, the small mass and size of hydrogen atoms enable them to easily migrate within the relatively rigid Si matrix, resulting in some metastable structural evolution known as *Staebler Wronski Effect* (SWE)²⁷. However, the role of hydrogen on electronic and optical properties in a-Si: H remains unexplored.

Here, we present a novel approach to generating amorphous structures of silicon from SiH₄ with hydrogen dilution by the RF-PECVD technique and reveal the detailed evolution of the electronic structure in creating

¹Department of Physics, Institut Teknologi Sepuluh Nopember, Surabaya 60111, Indonesia. ²Department of Electrical Engineering, Pertamina University, Jakarta 12220, Indonesia. ³Department of Physics, National University of Singapore, Singapore 117542, Singapore. ⁴Singapore Synchrotron Light Source, 5 Research Link, Singapore 117603, Singapore. ✉email: darminto@physics.its.ac.id; andriwo.rusydi@nus.edu.sg

Sample	Substrates	Hydrogen dilution (H ₂ /SiH ₄)	Silane concentration (%)	Chamber pressure (mTorr)	Power RF (watt)	Substrates temperature (°C)	Deposition time (min)
R-0	ITO	0	100	2000	10	270	30
R-16	ITO	16	5.9	2000	10	270	30
R-36	ITO	36	2.7	2000	10	270	30

Table 1. Deposition parameters for the (R-0 to R-36) layers used in solar cell.

exciton and plasmon coupling and their relationship to the performance of photovoltaic devices. We obtain an accurate physical model of the optical response and structures of a-Si: H by using spectroscopic ellipsometry.

Methods

The a-Si: H thin layer is intrinsically deposited on corning 1737 glass and ITO substrates employing the RF-PECVD, (MVSystem Inc. USA) technique in key-based UHV space loads with a key electrode area of 19.62 cm² and 4 cm electrode separation. The total deposition time for each film is kept constant for 30 min. The deposition parameters for the dilution of hydrogen SiH₄/H₂ are 0, 16, and 36 using RF power of 10 W, substrate temperature of 270 °C, and process pressure (PP) of 2000 mTorr, as presented in Table 1. The R-0 film (without hydrogen dilution) deposition is carried out during precipitation, while the R-16 and the R-36 films are deposited with hydrogen dilution in 30 min. The atomic force microscope (Agilent 5500) is used to study the surface morphology and roughness of the films. The dark and photoconductivity of the films are measured under vacuum (~10⁻⁵ mbar) in coplanar geometry, at the temperature range of 300–475 K, to estimate the activation energy.

Spectroscopic ellipsometry parameters ψ and Δ (viz., the ratio of the amplitude and phase difference between p- and s-polarized reflected light, respectively) are collected at 50°, 60°, and 70° angles of incidence, with the photon energy range between 0.6 and 6.5 eV using the measuring apparatus (V-VASE, J. A. Woollam Co.) with a rotating analyzer and a compensator at the Singapore Synchrotron Light Source (SSLS). The measurements are performed in ultrahigh vacuum chamber, which allows a clean surface to be measured²⁸ and a universal fitting is performed within the same optical parameters. Details of the instrument and the measurement geometry are described elsewhere²⁹. The real and imaginary parts of the dielectric constant $\langle \epsilon_1 \rangle$ and $\langle \epsilon_2 \rangle$ are extracted using a least-squares regression analysis³⁰ and an unweighted root-mean-square error function by fitting the experimental spectra with Woollam Complete Ease software. The parameters corresponding to the surface roughness of the R-0, R-16, and R-36 samples and the parameter of the respective dielectric functions are evaluated by a combination of the Tauc-Lorentz (TL)/Tauc-Lorentz + G model to determine thickness, band gap and optical constants of the films.

The following equations are used to evaluate the dielectric properties for the current set by a-Si: H³¹.

- (1) Complex dielectric function $\epsilon(\omega) = \epsilon_1(\omega) + i\epsilon_2(\omega)$ (ω = angular frequency of the incident photon).
- (2) Refractive index $n(\omega) = \sqrt{\frac{1}{2}[\sqrt{\epsilon_1^2(\omega) + \epsilon_2^2(\omega)} + \epsilon_1(\omega)]}$.
- (3) Extinction coefficient $\kappa(\omega) = \sqrt{\frac{1}{2}[\sqrt{\epsilon_1^2(\omega) + \epsilon_2^2(\omega)} - \epsilon_1(\omega)]}$.
- (4) Loss-function $-\text{Im}[\epsilon^{-1}(\omega)] = \frac{\epsilon_2(\omega)}{[\epsilon_1^2(\omega) + \epsilon_2^2(\omega)]}$.
- (5) Normal incident reflectivity $R(\omega) = \frac{[n(\omega) - 1]^2 + \kappa^2(\omega)}{[n(\omega) + 1]^2 + \kappa^2(\omega)}$.
- (6) Optical conductivity $\sigma_1(\omega) = \epsilon_0 \epsilon_2(\omega) \omega$ (ϵ_0 is the free-space permittivity).

For microscopy study using transmission electron microscope (TEM), all films are scratched and sonicated in acetone for several minutes and dispersed on a copper net. The high resolution- transmission electron microscopy (HR-TEM) images and selected area electron diffraction (SAED) patterns are recorded using JEOL-2100.

Results and discussion

Figure 1a shows that there are two exciton peaks, namely $E_{x-1} = 3.4$ eV and $E_{x-2} = 4.24$ eV with a wide energy shift between E_{x-1} and E_{x-2} of 0.84 eV originating from c-Si measurements using spectroscopic ellipsometry. For R-0 film in Fig. 1b, the exciton of both is pushed to the spectral weight at low energy and seen that there is a widening at $\langle \epsilon_2 \rangle$ from $E_{x-1} = 3.34$ eV and $E_{x-2} = 3.82$ eV with a magnitude of energy shift of 0.48 eV, so that the quantum confinement effect occurs with the transmission changing from high energy, crossing zero to lower energy³². Furthermore, it is important that there is spectral weight transfer at $\langle \epsilon_2 \rangle$ of the R-0 film, but is unseen in one of c-Si. It turns out that the peak in $\langle \epsilon_2 \rangle$ of the c-Si film occurs at high energy, namely at $E_1 = 5.34$ eV. There is a transfer of spectral to lower energy at E_0 of 3.32 eV, which causes a spectral weight transfer of 3 eV, which is a signature of electronic correlation. Figure 1c depicts the $\langle \epsilon_2 \rangle$ curve of the R-16 film, showing not only the quantum confinement effect, but also the dramatic effect of hydrogen. It is seen that both exciton peaks shift to each other and collapse to be one exciton. When more hydrogen is added, as the R-36 film in Fig. 1d, there is another shift of 0.84 eV in the $\langle \epsilon_2 \rangle$ curve between $E_{x-1} = 3.52$ eV and $E_{x-2} = 4.36$ eV. It leads to a rechanging exciton feature, which is somewhat the same as that of the c-Si film. This means that the hydrogen dilution has taken an important role in tuning the electronic structure of the deposited a-Si film.

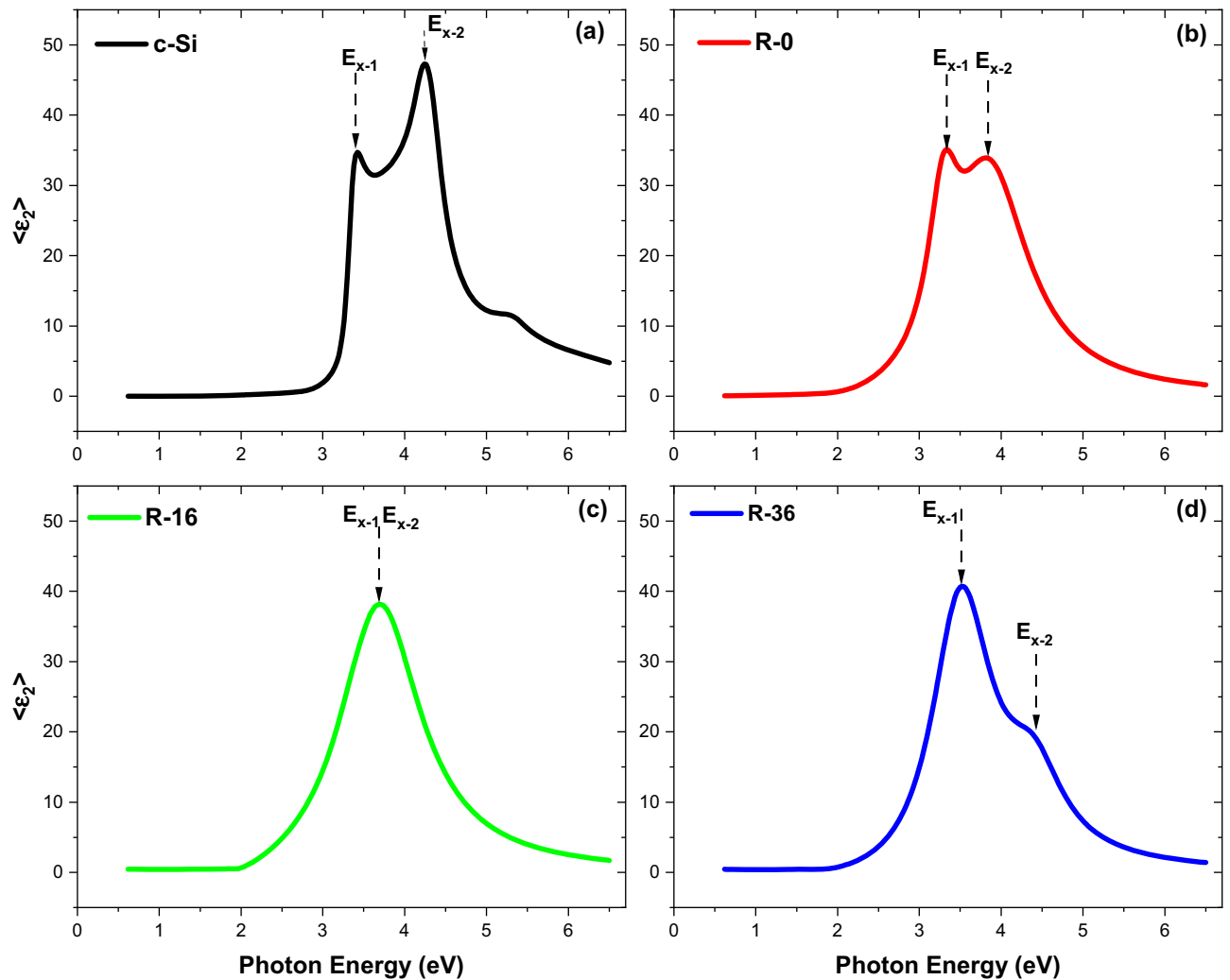


Figure 1. Imaginary part of complex dielectric function (E_{x-1} : conventional exciton, E_{x-2} : resonant excitons) $\langle \epsilon_2 \rangle$ (a) c-Si, (b) R-0, (c) R-16, and (d) R-36.

Figure 2 displays the real part $\langle \epsilon_1 \rangle$ of the complex dielectric function, loss function, and reflectivity of c-Si, R-0, R-16, and R-36 films. The value of $\langle \epsilon_1 \rangle$ changes dramatically from positive to negative, showing different type of plasmons (Fig. 2a–d) as further discussed later. The $\langle \epsilon_1 \rangle$ reaches a minimum with a positive value at about ~ 4.45 eV. For all films, $\langle \epsilon_2 \rangle$ exhibits a peak at ~ 3.34 eV and the rise is a characteristic of silicon, featuring a resonant exciton. Resonant excitonic effects are typically occurred above the optical band gaps due to strong electron–hole and electron–electron interactions and have been observed in graphene^{33–38}. The substrate also has non-reflective characteristics at ~ 1.00 eV but exhibits non-zero reflectivity at ~ 4.00 eV in Fig. 2e–h. When the a-Si: H film is deposited on the substrate, the reflectivity approaches zero and shows a depth at ~ 4.00 eV, shifting slightly with the addition of hydrogen. The minimum reflectivity at ~ 4.00 eV is a sign of plasmon.

The direct way to detect plasmons is via loss function³⁹ as shown in Fig. 2i–l. The loss function shows two peaks, at ~ 3.50 eV and ~ 5.20 eV. By combining loss function and $\langle \epsilon_1 \rangle$, we identify two different types of plasmons. For the former where $\langle \epsilon_1 \rangle$ is positive, it is unconventional, correlated plasmons²⁹. For the later, where $\langle \epsilon_1 \rangle$ is negative, it is conventional plasmons. The loss function curve does corroborate that the plasmon appears in the film³⁹, characterized by a peak at ~ 3.50 eV in Fig. 2i–l. The peaks show the red and blue shifts of ~ 0.74 eV respectively for the R-0 and R-36 films, which are consistent with the deep reflectivity. Another peak is also observed at 5.20 eV, implying that the plasmon is coupling with the exciton at this photon energy.

The macroscopic linear optical response of Si is represented by the complex dielectric function $\epsilon(\omega)$, which is closely related to the electronic band structure of the material. The structures observed in $\epsilon(\omega)$ are attributed to interband transitions as well as excitons at critical points, which can be analyzed in terms of standard analytic line shapes: $\epsilon(\omega) = C - Ae^{i\phi}(\omega - E + i\Gamma)^n$, where a critical point (CP) is described by the amplitude A , threshold energy E , broadening Γ , and the excitons phase angle ϕ . The exponent n has the value $-\frac{1}{2}$ for one-dimensional (1D), 0 logarithmic, i.e., $\ln(\omega - E + i\Gamma)$ for 2D, and $\frac{1}{2}$ for 3D CPs. Discrete excitons are represented by $n = -1$. The information obtained from the line-shape analysis can be compared with band structure calculations^{40–42}.

It is interesting to further review the appearance of excitons and plasmons in the samples. In the c-Si film, two resonant excitons (Fig. 1) and two plasmons (Fig. 2) are observed, consisting of a correlated plasmon (lower

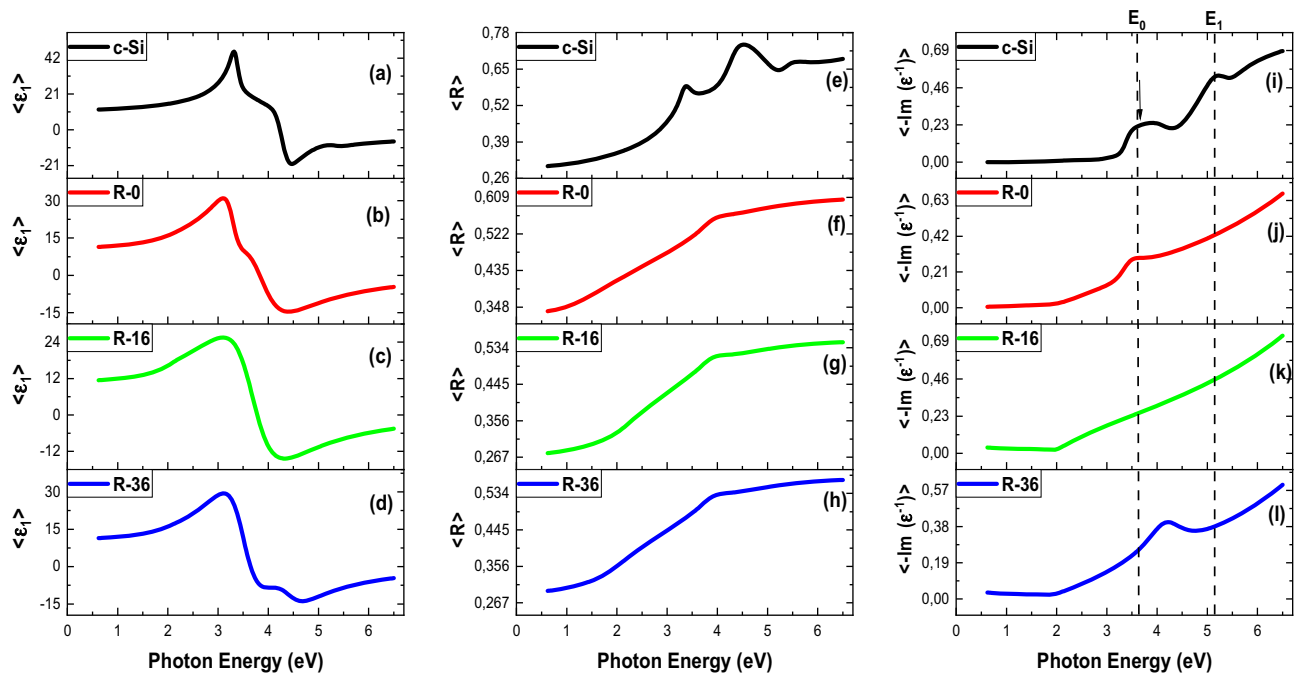


Figure 2. (a–d) Real part $\langle \epsilon_1 \rangle$ of the dielectric function, (e–h) reflectivity, and (i–l) loss function (E_0 : conventional plasmon, E_1 : correlated plasmons) c-Si, R-0, R-16, and R-36.

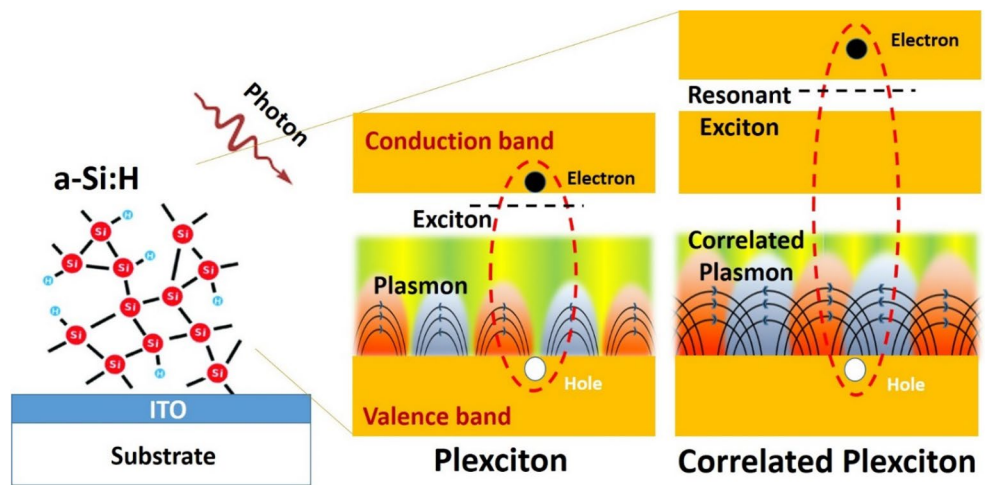


Figure 3. Schematic diagram of the coupling mechanism of correlated plasmon and resonant exciton.

energy) and a conventional plasmon (higher energy). The strong coupling between these two types of quasi-particles^{43–47}, constitutes the so-called plexciton. Since the plexciton in this study is a coupling between resonant exciton and correlated and/or conventional plasmons, we propose that this is a *correlated plexciton*. The correlated plexciton structures are observed to be persisted despite the detailed structure gradually changes in a-Si and a-Si:H, suggesting the importance of electronic correlations. As can be seen in Fig. 1, the two resonant excitons (E_{x1} and E_{x2}) undergo a shift in its energy closer to each other (R-0), merging into one exciton (R-16) and recover into two excitons again (R-36) in the presence of an increasing number of H atoms as illustrated in Fig. 3. On the other hand, the plasmons are still present in the whole a-Si samples, therefore, indicating that the presence of correlated plexciton could be confirmed.

To enhance the structure in the spectra and to perform a line-shape analysis of the CP, we calculate numerically the second derivative of the complex dielectric function with respect to photon energy $d^2\epsilon/d\omega^2$, as presented in Table 2. Figure 4 shows the experimental second-derivative spectrum of $\langle \epsilon_1 \rangle$, $\langle \epsilon_2 \rangle$, and loss function in the spectral regions where structures are observed (points). The solid and dotted lines represent the best fits to standard critical-point line shapes, derived from: $\frac{d^2\epsilon}{d\omega^2} = \begin{cases} n(n-1)Ae^{i\Phi}(\omega - E + i\Gamma)^{n-2}, & n \neq 0 \\ Ae^{i\Phi}(\omega - E + i\Gamma)^{-2}, & n = 0 \end{cases}$. The fit is per-

CP parameter	c-Si	R-0	R-16	R-36
E_{x-1} (eV)	3.40	3.34	3.66	3.52
E_{x-2} (eV)	4.24	3.82	3.66	4.36
E_0 (eV)	3.32	3.20	3.66	3.52
E_1 (eV)	3.80	3.76	3.66	3.52
E_2 (eV)	4.60	4.70	4.20	4.36
E_1' (eV)	5.34	4.95	4.20	4.36

Table 2. Critical-point (CP) parameters used in the calculation of second derivatives.

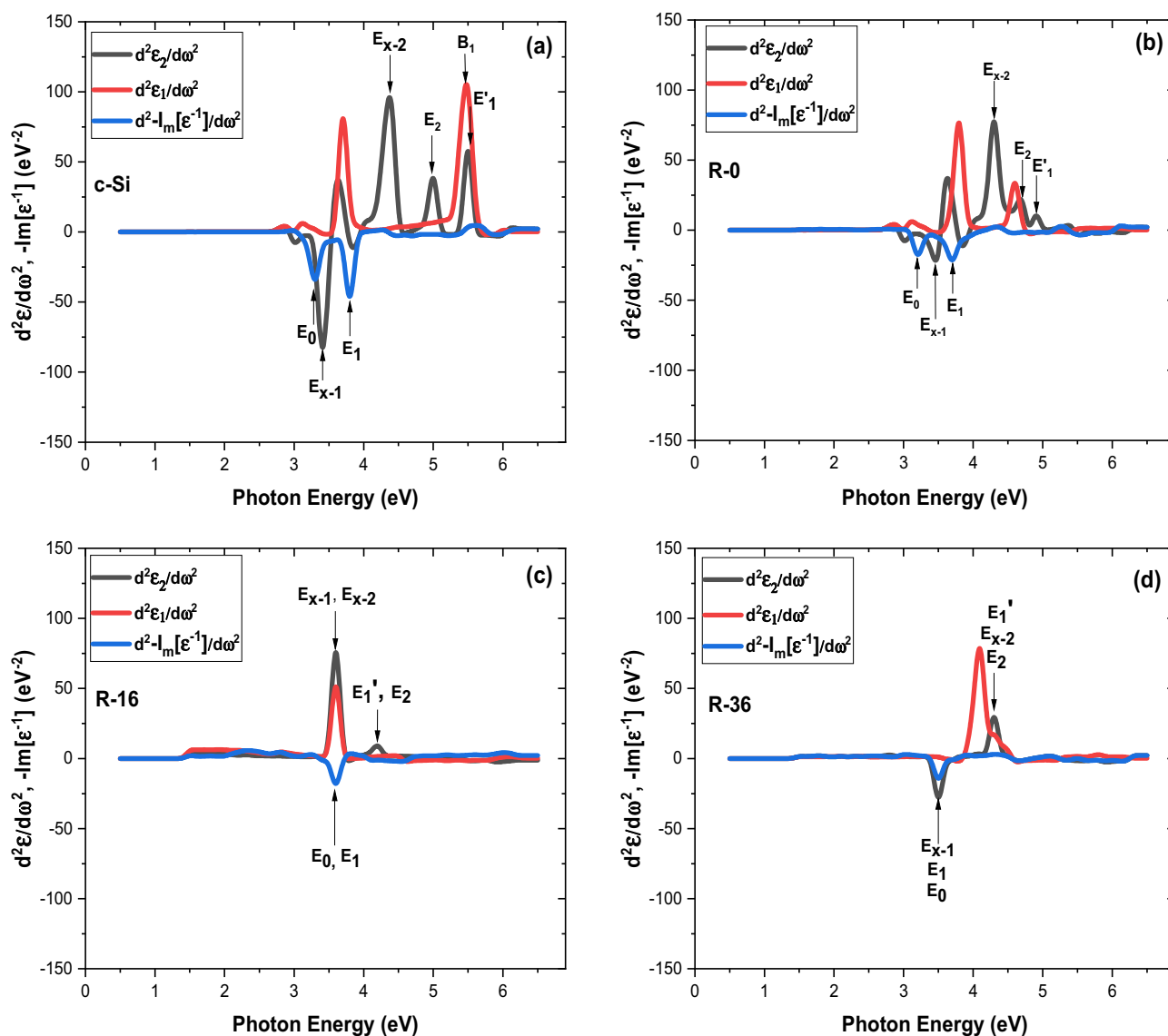


Figure 4. Fits to the second derivatives of the real (blue line) and imaginary (red line) parts complex dielectric function, include loss function of (a) c-Si, (b) R-0, (c) R-16, and (d) R-36.

formed simultaneously for the real and imaginary parts of $d^2\varepsilon/d\omega^2$ using a least-squares procedure^{48,49}. If the angle Φ in the phase factor $e^{i\Phi}$ take values, which are integer multiples of $\pi/2$, the line shape corresponds to transitions between uncorrelated one-electron bands while noninteger multiples are usually believed to include excitonic effects by allowing a mixture of two CP integer multiple line shapes.

Figure 5 shows a possible band scheme, where the valence band is positioned at 0 eV and the conduction band is positioned at ~ 4.00 eV. This placement is based on the assumption that the conduction band dissects the gap between the highest charged state and the lowest empty state (this gap is essentially the initial energy

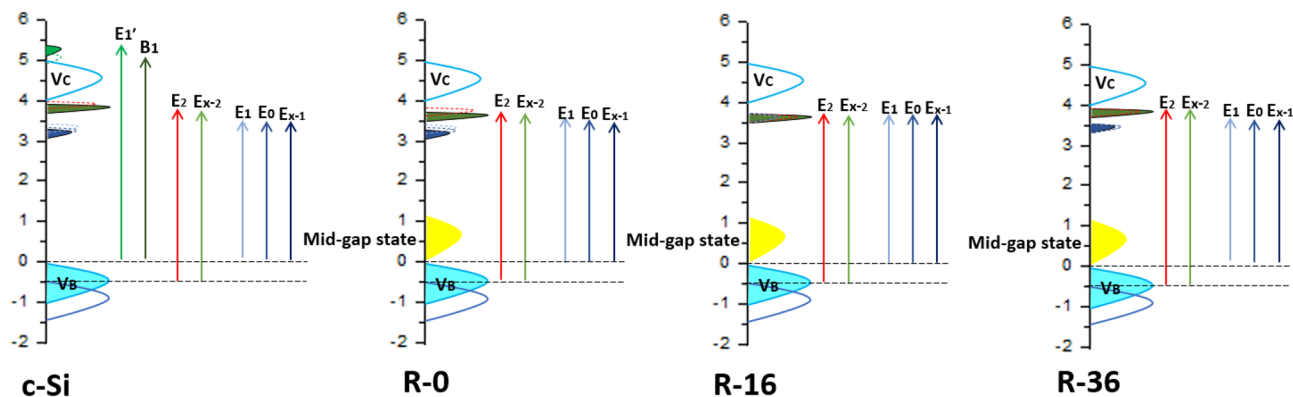


Figure 5. Schematic diagram of electronic band-structure in c-Si, R-0, R-16, and R-36.

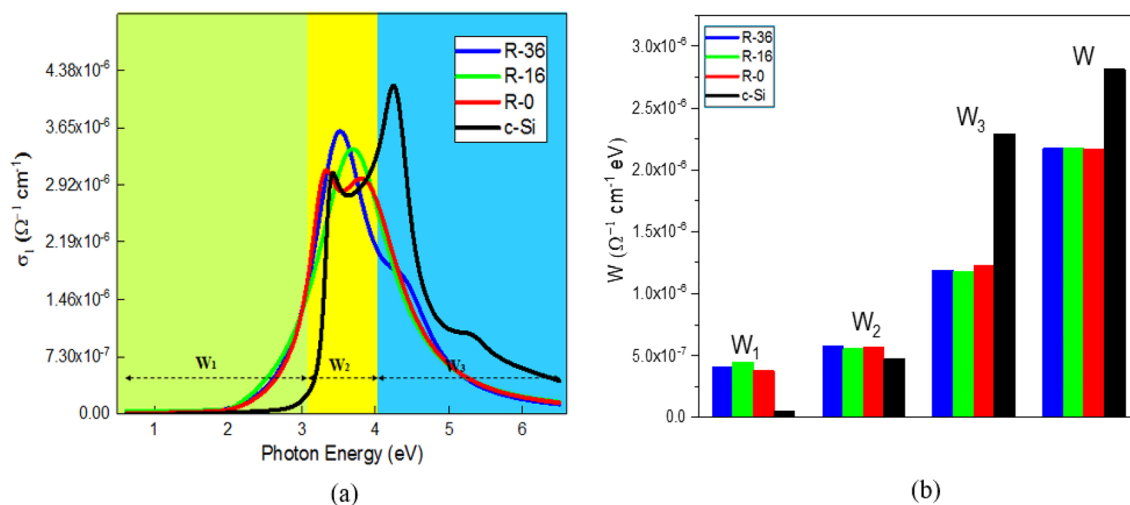


Figure 6. (a) Optical conductivity (σ_1) spectra, and (b) spectral weight of R-0, R-16, R-36 and c-Si. Inset: The estimated spectral weight transfer over three energy ranges: 0.6–3.1 eV (W_1), 3.1–4.0 eV (W_2), and 4.0–6.5 eV (W_3), while W is defined as $W_1 + W_2 + W_3$.

for the charge transfer process) in a 1:3 ratio, as seen from recent reports on c-Si. This estimation for the valence band position (i.e., 0 eV and below) is consistent with the < 1 eV gap between the valence band and conduction band in another recent calculation for c-Si⁵⁰. Based on the results of SE and second derivative analysis on the samples of c-Si, R-0, R-16 and R-36 that, at room temperature, a new midgap state is formed on the addition of H as illustrated in Fig. 5. Taking into account the fact that the system is not an ordinary semiconductor, we propose two new midgap states: one in the filled state and the other in the empty state with a very small finite gap in between. From the detailed observation of the electronic band structure, we imply that the unfilled middle gap state is likely to be formed by higher energy unfilled states, which fill the lower part of the conduction band. The proposed band structure also shows that, with the addition of H, the charge transfer transition tends to dominate the electron–hole transition, which is quantitatively confirmed by the spectral weight transfer⁵¹.

Since we are able to identify the optical transitions in the three a-Si: H, we can quantify the change in the optical transitions associated individually. This change is established quantitatively using the optical conductivity, $\sigma_1(\omega)$ of the a-Si: H because $\sigma_1(\omega)$ satisfies the f -sum (charge conservation) rule and is related to the total electron density n by the relation $\int_0^\infty \sigma_1(\omega) d\omega = \pi n e^2 / 2m_e$, where m_e is the rest mass of the electron⁵². For a finite-energy range, the integral can be expressed as $W = \int_{E_1}^{E_2} \sigma_1(E) dE$. The W is termed as the spectral weight transfer and is proportional to the *effective* number of electrons participating in the optical transitions within the energy range $[E_1, E_2]$. Considering the experimental energy range from 0.6 to 6.5 eV of our observed spectra, we divide the SWT into three different ranges, viz., W_1 for energy range 0.6–3.1 eV, W_2 for 3.1–4.0 eV, and W_3 for 4.0–6.5 eV. Estimated W_1 , W_2 , and W_3 and their sum W for each of the a-Si: H are shown in Fig. 6.

The total spectral weight W , from a-Si: H across the measured spectral range from 0.6 to 6.5 eV is shown in Fig. 6b. There is an increase in W when the sample adds hydrogen from R-16 to R-36, followed by a decrease to roughly the same level as in R-0 when the sample is missing hydrogen. These results indicate that there are more electrons with energies between 0.6 and 6.5 eV on R-36 than in R-0 and R-16. This means that in the R-36 sample, the number of electrons with energies beyond the measured spectral range increases. This spectral weight shift cannot be explained by the activation of the addition of a hydrogen atom only, because the energy

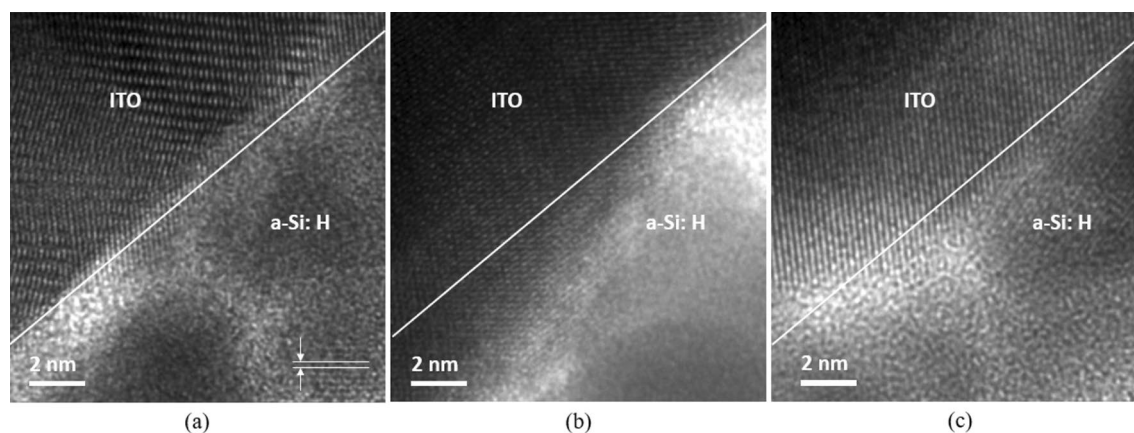


Figure 7. HR-TEM images of (a) R-0, (b) R-16, and (c) R-36 films, showing an evolution from nanocrystalline regime to amorphous phase due to hydrogen dilution.

associated with R-0 and R-16 is too small (< 33 meV); therefore, any extra energy gained or lost must come from the electron–electron correlation potential energy. Both plasmon and exciton couplings are seen in the R-0, dissipating at the R-16, which also coincides with the decrease in electron conductivity and electron density. Figure 6b shows the change in W for each of the three spectral regions of Fig. 6a when the sample adds hydrogen from R-16 to R-36. While there is little change in the low and medium energy regions, the spectral weight loss in the high-energy regions shows a significant shift in electron density from this spectral range to higher energies (above 6.5 eV). The increase in electron energies on the order of several eVs comes from the correlation of the long-distance electrons, which is now prominent due to decreased electronic filtering⁵³. This in turn gives rise to plasmonic activity, which is seen in conductive materials.

Given in Fig. 7 is the HR-TEM images of the films with different hydrogen content. A crystalline island having size of several nm can be observed in the R-0 film (Fig. 7a), exhibiting a strong proof in a nanocrystalline regime (nc-Si: H). The porous structure of the R-0 film is caused by the H_2 etching effect of the plasma. The inter-planar distance (d) calculated from the image is between 0.2 and 0.3 nm, corresponding to (111) and (220) planes in Si crystal. This can be attributed to the increased bonding and microstructure of these films subjected to hydrogen plasma. During the hydrogen treatment, a large flux of hydrogen atoms arriving at the surface of the film breaks the weak Si–Si bond and replaces it with a strong Si–Si bond⁵⁴. The hydrogen atoms also diffuse into most films and improve the structure of the film⁵⁵. During subsequent growth, Si atoms that arrive at the surface prefer to maintain this structural arrangement rather than forming a random network⁵⁶. This process continues for a few layers of atoms and a random network of Si atoms is then formed, which results in the growth of a-Si: H. For the R-16 in Fig. 7b, the film is only subjected to hydrogen plasma treatment once and subsequent precipitation for a longer period, which is not resulting in changes in the film’s microstructure. For the R-36 film, with higher H_2 dilution followed by shorter deposition time, the transformation from a-Si: H to nc-Si: H has resulted in a mixed phase of the amorphous and nano-crystalline structures, forming a denser amorphous film, as in Fig. 7c.

Conclusions

In summary, by simultaneously measuring the complex dielectric function, loss function, and reflectivity of the hydrogen dilution effect in the a-Si films using spectroscopic ellipsometry, we determine electronic and optical structures and observe an unusual spectral weight transfer resulting high-energy resonant excitons and correlated plasmons and significant shifts in Fermi levels. From the spectral weight transfer analysis, we find that after addition of hydrogen, a decrease in electronic screening causes an increase in long-range electron correlation and increases the potential energy of the system resulting in the formation of resonant excitons and correlated plasmons couplings, namely a *correlated* plexciton. The scattering of electrons from the coupling of high-energy resonant excitons and correlated plasmons results in an increase in bulk carrier density and, subsequently, a reversible shift in Fermi energy. Overall, we believe that the findings of this work can help boost the power conversion efficiency of solar cells with the demonstration results of high-energy resonant excitons and correlated plasmons for the performance of photovoltaic devices in a-Si: H, and the methodology introduced here can be used to investigate excitons and plasmons in semiconductors and strongly correlated electron systems.

Data availability

All data generated or analyzed during this study are included in this published article [and its Supplementary Information files].

Received: 1 August 2022; Accepted: 18 November 2022

Published online: 13 December 2022

References

- Yang, Z., Gao, P., Zhang, C., Li, X. & Ye, J. Scattering effect of the high-index dielectric nanospheres for high performance hydrogenated amorphous silicon thin-film solar cells. *Sci. Rep.* **6**, 30503 (2016).
- Despeisse, M. *et al.* Hydrogenated amorphous silicon sensor deposited on integrated circuit for radiation detection. *IEEE Trans. Nucl. Sci.* **55**, 802–811 (2008).
- Park, J. *et al.* High efficiency inorganic/inorganic amorphous silicon/heterojunction silicon tandem solar cells. *Sci. Rep.* **8**, 15386 (2018).
- Flewitt, A. J. Hydrogenated amorphous silicon thin film transistors (a Si: H TFTs). In *Handbook of Visual Display Technology* (eds Chen, J. *et al.*) 627–646 (Springer, 2012).
- Kim, H.-E., Jang, H.-W., Kim, G.-H., Kim, S.-K. & Yoon, S.-M. Improvement in mechanical durability of stretchable charge-trap memory transistors with engineered wavy-dimensional structures. *ACS Appl. Electron. Mater.* **2**, 2984–2993 (2020).
- Franco, A., Geissbühler, J., Wyrsh, N. & Ballif, C. Fabrication and characterization of monolithically integrated microchannel plates based on amorphous silicon. *Sci. Rep.* **4**, 4597 (2014).
- Brongersma, M. L., Cui, Y. & Fan, S. Light management for photovoltaics using high-index nanostructures. *Nat. Mater.* **13**, 451–460 (2014).
- Bhattacharya, S. & John, S. Beyond 30% Conversion efficiency in silicon solar cells: A numerical demonstration. *Sci. Rep.* **9**, 12482 (2019).
- Kim, S. *et al.* Improving the efficiency of rear emitter silicon solar cell using an optimized n-type silicon oxide front surface field layer. *Sci. Rep.* **8**, 10657 (2018).
- Qu, X. *et al.* Identification of embedded nanotwins at c-Si/a-Si: H interface limiting the performance of high-efficiency silicon heterojunction solar cells. *Nat. Energy* **6**, 194–202 (2021).
- Wen, X. *et al.* Vapor transport deposition of antimony selenide thin film solar cells with 7.6% efficiency. *Nat. Commun.* **9**, 2179 (2018).
- Liu, W. *et al.* Light-induced activation of boron doping in hydrogenated amorphous silicon for over 25% efficiency silicon solar cells. *Nat. Energy* **7**, 427–437 (2022).
- Sriraman, S., Agarwal, S., Aydil, E. S. & Maroudas, D. Mechanism of hydrogen-induced crystallization of amorphous silicon. *Nature* **418**, 62–65 (2002).
- Zhou, H. P. *et al.* Hydrogen-plasma-induced rapid, low-temperature crystallization of μm -thick a-Si: H films. *Sci. Rep.* **6**, 32716 (2016).
- Kasap, S., Koughia, C., Singh, J., Ruda, H. & O’Leary, S. Optical properties of electronic materials: Fundamentals and characterization. In *Springer Handbook of Electronic and Photonic Materials* (eds Kasap, S. & Capper, P.) 47–77 (Springer, 2007).
- Schulze, T. F. *et al.* Impact of a-Si: H structural properties on the annealing behavior of a-Si:H/c-Si heterostructures used as precursors for high-efficiency solar cells. *MRS Online Proc. Libr.* **1268**, 107 (2010).
- Zhao, L. *et al.* Plasma enhanced chemical vapor deposition of excellent a-Si: H passivation layers for a-Si:H/c-Si heterojunction solar cells at high pressure and high power. *Front. Energy* **11**, 85–91 (2017).
- Kim, J. *et al.* 10.5% efficient polymer and amorphous silicon hybrid tandem photovoltaic cell. *Nat. Commun.* **6**, 6391 (2015).
- Cao, E., Lin, W., Sun, M., Liang, W. & Song, Y. Exciton-plasmon coupling interactions: From principle to applications. *Nanophotonics* **7**, 145–167 (2018).
- Zhang, Z., Fang, Y., Wang, W., Chen, L. & Sun, M. Propagating surface plasmon polaritons: Towards applications for remote-excitation surface catalytic reactions. *Adv. Sci.* **3**, 1500215 (2016).
- Sazonov, A., Nathan, A. & Striakhilev, D. Materials optimization for thin film transistors fabricated at low temperature on plastic substrate. *J. Non-Cryst. Solids* **266–269**, 1329–1334 (2000).
- Ren, N. *et al.* Controlling performance of a-Si: H solar cell with SnO₂: F front electrode by introducing dual p-layers with p-a-SiOx:H/p-nc-SiOx: H nanostructure. *Sol. Energy* **171**, 907–913 (2018).
- Wilken, K., Güneş, M., Wang, S., Finger, F. & Smirnov, V. Understanding the origin of thermal annealing effects in low-temperature amorphous silicon films and solar cells. *Phys. Status Solidi A* **219**, 2100451 (2022).
- de Jong, M. M. *et al.* Utilization of geometric light trapping in thin film silicon solar cells: Simulations and experiments. *Prog. Photovolt. Res. Appl.* **22**, 540–547 (2014).
- Camargo, S. S., Carreño, M. N. P. & Pereyra, I. Hydrogen effusion from highly-ordered near-stoichiometric a-SiC:H. *J. Non-Cryst. Solids* **338–340**, 70–75 (2004).
- Beyer, W. Diffusion and evolution of hydrogen in hydrogenated amorphous and microcrystalline silicon. *Sol. Energy Mater. Sol. Cells* **78**, 235–267 (2003).
- Guo-gang, Q. & Guang-lin, K. A new model for the Staebler–Wronski effect. *Philos. Mag. Lett.* **57**, 117–122 (1988).
- Gogoi, P. K. *et al.* Oxygen passivation mediated tunability of trion and excitons. *Phys. Rev. Lett.* **119**, 077402 (2017).
- Whitcher, T. J. *et al.* Correlated plasmons in the topological insulator Bi₂Se₃ induced by long-range electron correlations. *NPG Asia Mater.* **12**, 1–9 (2020).
- Asmara, T. C., Santos, I. & Rusydi, A. Self-consistent iteration procedure in analyzing reflectivity and spectroscopic ellipsometry data of multilayered materials and their interfaces. *Rev. Sci. Instrum.* **85**, 123116 (2014).
- Chaudhuri, A. *et al.* Quasilocals plasmons in the insulator-metal transition in the Mott-type perovskites. *Phys. Rev. B* **98**, 165303 (2018).
- Gogoi, P. K. *et al.* Anomalous excitons and screenings unveiling strong electronic correlations in. *Phys. Rev. B* **92**, 035119 (2015).
- Yang, L., Deslippe, J., Park, C.-H., Cohen, M. L. & Louie, S. G. Excitonic effects on the optical response of graphene and bilayer graphene. *Phys. Rev. Lett.* **103**, 186802 (2009).
- Bartolomé, J. *et al.* Highly quenched orbital moment in textured Fe-phthalocyanine thin films. *Phys. Rev. B* **81**, 195405 (2010).
- Santos, I. *et al.* Observation of room-temperature high-energy resonant excitonic effects in graphene. *Phys. Rev. B* **84**, 081403 (2011).
- Alexeev, E. M. *et al.* Resonantly hybridized excitons in moiré superlattices in van der Waals heterostructures. *Nature* **567**, 81–86 (2019).
- Kojima, O., Kita, T., Steer, M. J. & Hogg, R. A. Resonant exciton excitation photoluminescence and dynamics in a GaAs/AlAs multiple quantum well with internal electric field. *AIP Adv.* **10**, 095016 (2020).
- Reichardt, S. & Wirtz, L. Nonadiabatic exciton-phonon coupling in Raman spectroscopy of layered materials. *Sci. Adv.* **6**, 5915 (2020).
- Asmara, T. C. *et al.* Tunable and low-loss correlated plasmons in Mott-like insulating oxides. *Nat. Commun.* **8**, 15271 (2017).
- Adachi, S., Mori, H. & Ozaki, S. Model dielectric function for amorphous semiconductors. *Phys. Rev. B* **66**, 153201 (2002).
- Johansson, M. B., Zietz, B., Niklasson, G. A. & Österlund, L. Optical properties of nanocrystalline WO₃ and WO_{3-x} thin films prepared by DC magnetron sputtering. *J. Appl. Phys.* **115**, 213510 (2014).
- Hikino, S. & Adachi, S. Structural changes in ion-implanted and rapid thermally annealed Si(100) wafers studied by spectroscopic ellipsometry. *J. Phys. Appl. Phys.* **37**, 1617 (2004).
- Mu, X. & Sun, M. Interfacial charge transfer exciton enhanced by plasmon in 2D in-plane lateral and van der Waals heterostructures. *Appl. Phys. Lett.* **117**, 091601 (2020).

44. Chen, Y., Cheng, Y. & Sun, M. Nonlinear plexitons: Excitons coupled with plasmons in two-photon absorption. *Nanoscale* **14**, 7269–7279 (2022).
45. Cao, Y. & Sun, M. Perspective on plexiton based on transition metal dichalcogenides. *Appl. Phys. Lett.* **120**, 240501 (2022).
46. Yin, X. *et al.* Excitons: Modulation of new excitons in transition metal dichalcogenide-perovskite oxide system. *Adv. Sci.* **6**, 1970073 (2019).
47. Chaudhuri, A. *et al.* Direct observation of anisotropic small-hole polarons in an orthorhombic structure of films. *Phys. Rev. B* **97**, 195150 (2018).
48. Omri, M., Sayari, A. & Sfaxi, L. Fabrication and characterization of multi-layer InAs/InGaAs quantum dot p-i-n GaAs solar cells grown on silicon substrates. *Appl. Phys. Mater. Sci. Process.* **124**, 74 (2018).
49. Asmara, T. C. *et al.* Large spectral weight transfer in optical conductivity of SrTiO₃ induced by intrinsic vacancies. *J. Appl. Phys. Lett.* **115**, 213706 (2014).
50. Santoso, I. *et al.* Optical and electronic structure of quasi-freestanding multilayer graphene on the carbon face of SiC. *Europhys. Lett.* **108**, 37009 (2014).
51. Radha, S. K. *et al.* Optical response and band structure of including electron-hole interaction effects. *Phys. Rev. B* **104**, 115120 (2021).
52. Gogoi, P. K. *et al.* Optical conductivity study of screening of many-body effects in graphene interfaces. *Europhys. Lett.* **99**, 67009 (2012).
53. Ye, L. H. *et al.* Anomalous spectral-weight transfers unraveling oxygen screening and electronic correlations in the insulator-metal transition of VO₂. *Phys. Rev. B* **91**, 081112 (2015).
54. Choi, S. *et al.* Formation and suppression of hydrogen blisters in tunnelling oxide passivating contact for crystalline silicon solar cells. *Sci. Rep.* **10**, 9672 (2020).
55. Kalas, B. *et al.* Micro-combinatorial sampling of the optical properties of hydrogenated amorphous for the entire range of compositions towards a database for optoelectronics. *Sci. Rep.* **10**, 19266 (2020).
56. Dong, Z. *et al.* Ultraviolet interband plasmonics with Si nanostructures. *Nano Lett.* **19**, 8040–8048 (2019).

Acknowledgements

The authors acknowledge the support by the Ministry of Education and Culture of the Republic of Indonesia for providing the Indonesian Scholarship and the World Class Professorship. The works at the National University of Singapore were supported by the Singapore Ministry of Education (T2EP50220-0041 and MOE2019-T2-1-037). The authors would like to acknowledge the ITS Research Center and the Singapore Synchrotron Light Source (SSLS) for providing the facility necessary for conducting the research. The SSLS is a National Research Infrastructure under the National Research Foundation Singapore.

Author contributions

Y.C. and D. proposed the idea and discussed about the results, S.P. and M.A.N. carried out the experiments, R.A., B.P., and M.A.B. wrote the manuscript and revised by D. and A.R., and A.R. and D. provided the insight of the experimental data coherently and proposed the correlated plexiton.

Competing interests

The authors declare no competing interests.

Additional information

Supplementary Information The online version contains supplementary material available at <https://doi.org/10.1038/s41598-022-24713-5>.

Correspondence and requests for materials should be addressed to D. or A.R.

Reprints and permissions information is available at www.nature.com/reprints.

Publisher's note Springer Nature remains neutral with regard to jurisdictional claims in published maps and institutional affiliations.



Open Access This article is licensed under a Creative Commons Attribution 4.0 International License, which permits use, sharing, adaptation, distribution and reproduction in any medium or format, as long as you give appropriate credit to the original author(s) and the source, provide a link to the Creative Commons licence, and indicate if changes were made. The images or other third party material in this article are included in the article's Creative Commons licence, unless indicated otherwise in a credit line to the material. If material is not included in the article's Creative Commons licence and your intended use is not permitted by statutory regulation or exceeds the permitted use, you will need to obtain permission directly from the copyright holder. To view a copy of this licence, visit <http://creativecommons.org/licenses/by/4.0/>.

© The Author(s) 2022